Internal Model Control for Spiral Trajectory Tracking With MEMS AFM Scanners

Ali Bazaei, *Member, IEEE*, Mohammad Maroufi, *Student Member, IEEE*, Anthony G. Fowler, *Member, IEEE*, and S. O. Reza Moheimani, *Fellow, IEEE*

Abstract—We demonstrate the application of internal model control for accurate tracking of spiral scan trajectories, where the reference signals are orthogonal sinusoids whose amplitudes linearly vary with time. The plant is a 2-D microelectromechanical system nanopositioner equipped with *in situ* differential electrothermal sensors and electrostatic actuators. This device is used as the scanner stage in an atomic-force microscope. Additional internal model components are included in the controllers to compensate for the residual tracking errors due to plant nonlinearities. In a large scan range with a diameter of 16 μm, we achieved tracking of 1430-Hz spiral sinusoids, a frequency beyond the undamped fundamental resonance of the plant at 1340 Hz. This leads to a video-rate scan speed of 18 frames/s.

Index Terms—Atomic-force microscope (AFM) imaging, internal model control, microelectromechanical (MEMS) nanopositioner, spiral scan.

I. INTRODUCTION

THERE has been growing research interest in the miniaturization of scanning probe microscopy (SPM) using microfabrication and MEMS technologies [1]–[5]. This is motivated by a reduction in fabrication cost, high image resolution, fast operation, and other applications such as data storage [6]–[9].

In SPM, raster scan methods are usually used, where triangular trajectories are employed to sweep the sample area [10], [11]. Compared with smooth trajectories such as spiral [12], cycloid [13], and Lissajous patterns [14], [15], triangular waveforms contain strong harmonic components due to their repetitive rate discontinuities. Hence, accurate tracking of a triangular reference in a raster scan method generally requires a higher closed-loop bandwidth than that of a nonraster scan approach [13], [14], [16].

Flexure-guided nanopositioners are generally used in atomic-force microscope (AFM) scanning stages to achieve high positioning resolutions and scan speeds within the

actuation limits [17]. However, such structurally flexible mechanisms have lightly damped resonance modes, limiting the stability margins and closed-loop bandwidth of the feedback systems designed to track the scan pattern waveforms [18]. Considering the limited bandwidth of AFM scanners and the strong harmonic content of triangular waveforms, we can significantly improve the imaging speed by applying smooth scan pattern trajectories rather than the common raster scan method.

Compared with other scan pattern trajectories such as cycloids and Lissajous patterns, the spiral scan method is the most effective at not retracing any part of the targeted area, making it a strong candidate to achieve the highest imaging rate. In addition, the spacings between adjacent scan lines are identical in the spiral pattern, which provides a uniform and well defined image resolution at each point of the scan area. However, the reference signals required to generate spiral patterns are sinusoids with time-varying amplitudes, which are harder to track than the constant amplitude references used in cycloid and Lissajous patterns. The control methods used so far for spiral scan, such as positive position feedback [16], [19], linear quadratic Gaussian (LQG) [20], multi-input multioutput model predictive control [21], and phase-locked loop [22], achieved acceptable tracking performances at reference frequencies below 20% of the scanner resonance frequency. In addition, due to the time-varying amplitude of the spiral reference, even if the plant were free from nonlinearities and measurement noise, the foregoing control methods could not asymptotically converge the tracking error to zero.

Internal model control is a well-established approach for asymptotic tracking and/or rejection of exogenous signals, which can provide zero steady-state error subject to the stability of the feedback loop and linearity of the plant [23]. This method has recently been applied for tracking of sinusoids with constant amplitudes in a Lissajous AFM scan method [14], [24]. However, the effective application of internal mode control to AFM imaging with a spiral pattern has not been reported yet. This is probably due to the marginally stable poles of internal mode controllers (IMCs) along with highly undamped resonance modes of scanners, making the tuning of controller parameters for desired closed-loop performance and stability margins more challenging.

In this paper, we introduce a systematic procedure to design IMCs for tracking of spiral trajectories in a MEMS AFM nanopositioner with a significant improvement in control and scan speed compared with the past methods. Our objective

Fig. 1. SEM images of the MEMS nanopositioner.

Fig. 2. Excitation circuit used for the comb drive actuators on the x-axis. After being amplified by a factor of 4 ($v_{ix} = 4v_x$) and augmented by a quiescent voltage of V_q, the actuation signal v_x is applied to the comb drives with opposite signs. A similar actuation scheme is used for the y-axis with an independent actuation signal denoted by v_y.

Fig. 3. Readout circuit for electrothermal sensor of x-axis. A pair of MEMS heaters is actuated by a constant bias voltage. Displacement x of the heat sink induces opposite variations in the resistances of the heaters. The difference between the heater resistances is amplified as an output voltage proportional to displacement. A similar sensing method is also used for the y-axis.

is to design proper IMCs with the smallest degree. We start from the simplest IMC structure and gradually increase the controller degree to achieve the desired tracking performance.

The remainder of the paper continues as follows. In Section II, we describe the fabricated MEMS nanopositioner with its built-in position sensing and actuation circuitry, where the open-loop response and its variations due to aging are also discussed. To alleviate the highly resonant response of the plant without increasing the order of the system, we design a simple damping compensator in Section III. In Section IV, we briefly present the characteristics of the reference signals for generation of the spiral trajectory. The proposed minimal-order IMCs for spiral scan trajectories are presented in Section V. We describe the resulting AFM images obtained by the proposed control in Section VI. We finally summarize the achievements in Section VII.

II. DESCRIPTION OF THE MEMS NANOPOSITIONER

Fig. 1 shows an SEM image of the MEMS nanopositioner, micromachined through a standard Silicon on Insulator-MEMS fabrication process [25]. The suspended scan table in the middle can be displaced along the x and y directions through the suspension beams (type B) attached to the movable electrodes of electrostatic actuators. Upon the application of a voltage across a stator comb w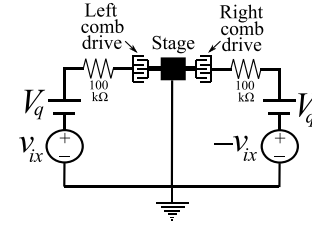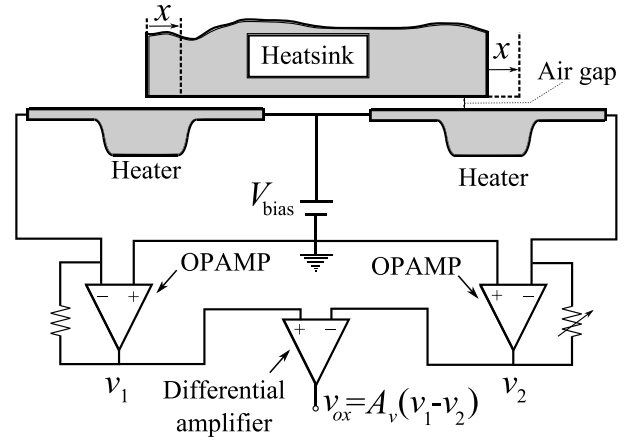ith the movable comb grounded, the scan table is displaced by an electrostatic attractive force toward the stator comb. It is then displaced by tensile forces exerted on the type B suspensions, while the stage suspensions on the orthogonal axis easily deflect due to their smaller stiffness. The tensile nature of the force on Type B suspensions ensures that no buckling happens and their high stiffness along the actuation direction makes the displacements of the driving comb and stage nearly identical. To minimize any possible rotational motion, the displacement of each movable comb is restricted along the x or y direction by longer suspension beams (type A) attached to the fixed frame. Further details on this nanopositioner, including its mechanical specifications and design, are reported in [26].

Having two opposing comb drives for each axis enables us to apply the differential actuation scheme shown in Fig. 2, which considerably linearizes the force–voltage characteristic of the actuator compared with the quadratic characteristic of a single comb drive [9], [27]. To measure the stage displacements along the x- and y-axis, we use differential electrothermal sensors with shaped heaters. These sensors provide a 4.5-kHz sensing bandwidth, which is well beyond the 0.7-kHz mechanical bandwidth of the nanopositioner [26], [28]. Fig. 3 shows the schematic of the x-axis readout circuit, where displacement x is proportional to the output voltage v_{ox}.
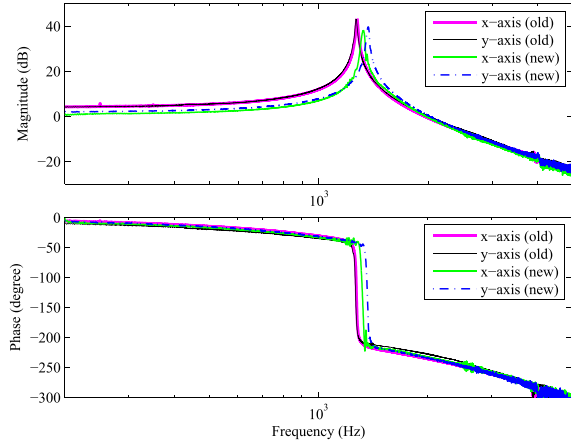
Fig. 4. Experimental open-loop frequency responses of each individual axis of the nanopositioner from actuation input v_x/v_y to sensor output v_{ox}/v_{oy}. The old results were obtained 8 months earlier than the new results.

A. Open-Loop Response and Uncertainties

With bias voltages of $V_q = 40$ V and $V_{bias} = 5$ V in the actuator and sensor circuits, we obtain the experimental frequency response of each individual channel from the actuation input of one axis to the sensor output of the same axis, as shown in Fig. 4. To characterize uncertainties in the dynamics of the device arising from aging, we have also included in Fig. 4 the system response with the same actuation and sensor settings obtained 8 months earlier [7]. These measurements indicate an increase in resonance frequency from 1270 Hz to almost 1343 Hz (6%), a decrease in low frequency gain from 1.6 to almost 1.3 (19%), and a reduction in the Q factor from 90 to almost 60 (33%). Moreover, new characterizations of the sensors by a Polytec MSA-050-3D micro system analyzer indicate that their calibration factors, denoted by c_x and c_y, have been reduced from almost 0.73 to 0.63 V/μm (14%).

For consistency with the original results, we include a gain of $(1.6/1.3) = 1.23$ in series with each actuation input to have almost the same open-loop dc gain as before. Using a least-squares identification method, we obtain the following model, which adequately approximates the open-loop experimental frequency responses of both axes, as shown in Fig. 5:

$$P(s) = 1.6 \frac{\frac{(s-25713)^2+30425^2}{25713^2+30425^2}}{\left(1+\frac{s}{20383}\right)\left[\frac{(s+41)^2+8419^2}{41^2+8419^2}\right]}. \qquad (1)$$

III. DAMPING LOOP

Before designing the IMCs, it is very helpful to damp the highly resonant dynamics of the nanopositioner [14], [24]. IMCs designed to track sinusoids generally include marginally stable poles, which together with the highly undamped modes of the plant may lead to instability, very small stability margins, or slow response in a single-loop design with a low-order controller. In most of the standard controller design methods such as pole assignment, H_∞, and LQG, the controller degree increases with the plant degree. Hence, it is important to
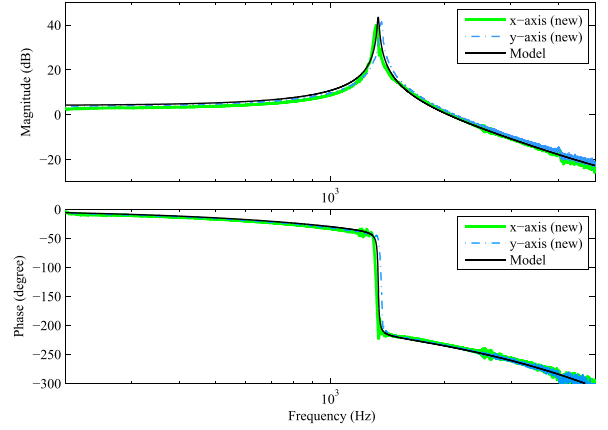

Fig. 5. Open-loop experimental frequency responses multiplied by a factor of 1.23 along with the Bode plot of the model.
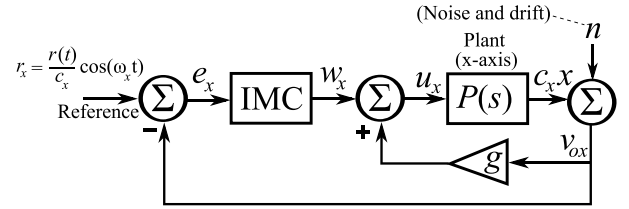

Fig. 6. Block diagram of the control system for x-axis of the nanopositioner. A similar system is also applied to control the y-axis.
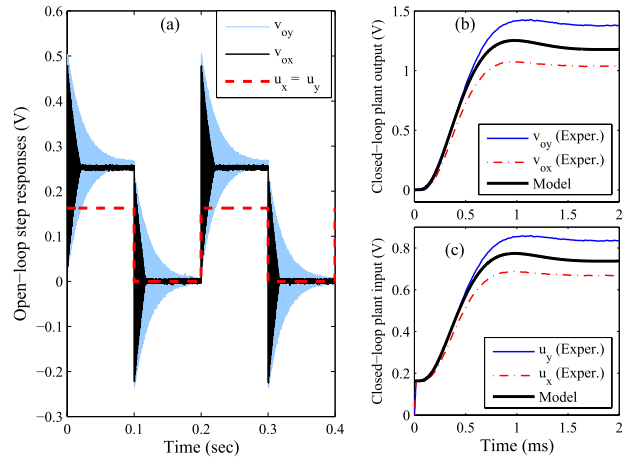
Fig. 7. (a) Open-loop experimental step responses of the plant. (b) and (c) Closed-loop experimental step responses of the inner loop along with that of the model, while the outer loop is open and a step with height of 0.1626 V is applied at w_x and w_y (corresponding to an almost 400-nm steady displacement).

keep the degree of the damping controller small to obtain proper IMCs with minimum degrees. We apply the simplest form of damping controller, which is a constant gain of $g = 0.4878$ with positive feedback, as shown by the inner feedback loop in Fig. 6. To examine the damping performance of the inner loop, we applied a square-wave signal with a height of 0.1626 V to the open- and closed-loop systems. The resulting experimental open-loop step responses are shown in Fig. 7(a), indicating a highly resonant behavior whose settling time exceeds 200 ms. In spite of the applied linear actuation mechanism, the system still exhibits a nonlinear

behavior for the x-axis, which is a sharp reduction of vibration amplitude in about 20 ms. Fig. 7(b) and (c) shows the closed-loop experimental step responses of the inner loop, indicating a desirable damping performance with a settling time of less than 2 ms. Using (1) as the plant model, we have also included the simulated step response of the inner loop in Fig. 7(b) and (c), indicating a transient response similar to the experimental results. The difference between the closed-loop experimental and simulated results at steady-state can be explained by the difference between the dc gains of the plant model and the actual systems. From the steady state values in Fig. 7(b) and (c), the actual dc gains for the x- and y-axis are 1.55 and 1.65, respectively, which are slightly different from that of the model (1.6). Hence, the expected steady-state step responses of the inner loop for the x- and y-axis are $0.1626(1.55/1 - 1.55g) = 1.033$ and 1.375, respectively, rather than 1.1851 from the model. The damping loop has gain and phase margins of 2.16 dB and $-20°$, which are acceptable considering the desirable damping performance and the fact that the dc gains of the plant tend to decrease over time.

IV. SPIRAL TRAJECTORY

For the spiral scan, we consider the spiral of Archimedes traced at a constant angular velocity, which is generated through simultaneous tracking of the following *displacement* sinusoidal references:

$$d_x = r(t)\cos(\omega t), \quad d_y = r(t)\sin(\omega t) \tag{2}$$

along the x- and y-axis, respectively. During the scan, the amplitude $r(t)$ of the sinusoids linearly increases with time from an initial value r_i to a final value r_f as

$$r(t) = r_i + pft, \quad t \in [0, t_f] \tag{3}$$

where p is the pitch, i.e., the distance between two adjacent scan curves. Having selected the pitch, the scan period t_f is determined by

$$t_f = \frac{r_f - r_i}{pf}. \tag{4}$$

In our simulations and experiments, we opted for $r_i = 0.1 \ \mu$m, $r_f = 8 \ \mu$m, and $p = 0.1 \ \mu$m to generate a spiral trajectory with a diameter of 16 μm. In addition to a larger scan diameter, the selected pitch in this reference trajectory is deliberately much higher than those reported in [12], [16], and [20]–[22] to make the scan period much shorter. However, since the amplitudes of the sinusoids increase much faster, tracking of the selected reference is more challenging. The profiles of the references and the desired spiral trajectory are shown in Fig. 8.

We have also examined the tracking performance of the nanopositioner in open-loop conditions. To do this, we applied orthogonal spiral signals to the x and y actuation inputs with identical frequencies (600 Hz) but different amplitudes so that the resulting displacement outputs for each axis have almost the same maximum swing of $2r_f = 16 \ \mu$m. For each axis, we generated a reference signal proportional to the actuation signal so that the maximum swing is 16 μm as well. The results are shown in Fig. 9, confirming unacceptable magnitudes of the tracking errors and large deviations from the reference trajectory.
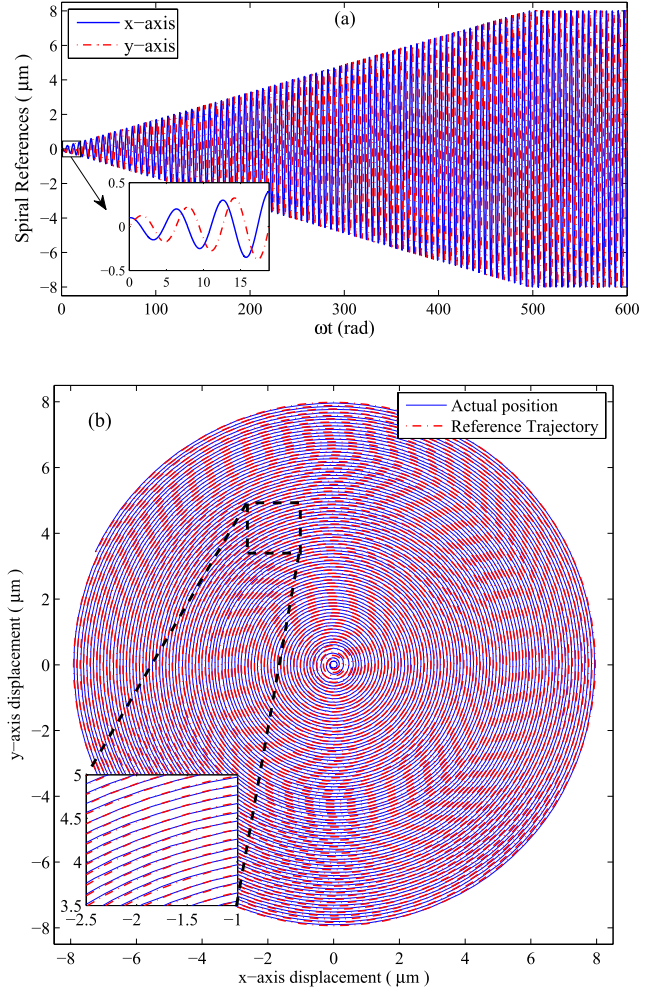

Fig. 8. (a) Profiles of spiral reference signals in a normalized time domain. (b) Reference trajectory and the actual trajectory of the stage when the final controller designed in Section V-B are used for both axes and the 600-Hz spiral references are applied simultaneously.

V. INTERNAL MODEL CONTROL

In this section, we present the design of IMCs, considering the damped system described in Section III as the plant, with the transfer function

$$G(s) = \frac{N(s)}{D(s)} = \frac{1456[(s - 25713)^2 + 30425^2]}{(s + 13375)[(s + 3190)^2 + 3687^2]}. \tag{5}$$

To ensure that the controller has the smallest possible degree, we start from the simplest IMC and include more modes in the controller to achieve the desired control performance. The desired values of 600, 1430, and 240 Hz are considered for the frequency of the sinusoids generating the spiral trajectory. For each frequency, we design an intermediate IMC $C_i(s)$ before designing the final IMC $C_f(s)$, which has a higher degree.

A. Intermediate Controller for 600 Hz

In spiral scans, the reference signals for the x and y coordinates are zero biased sinusoids with a frequency of $\omega = 2\pi f$ and slowly varying amplitudes. If the IMC includes
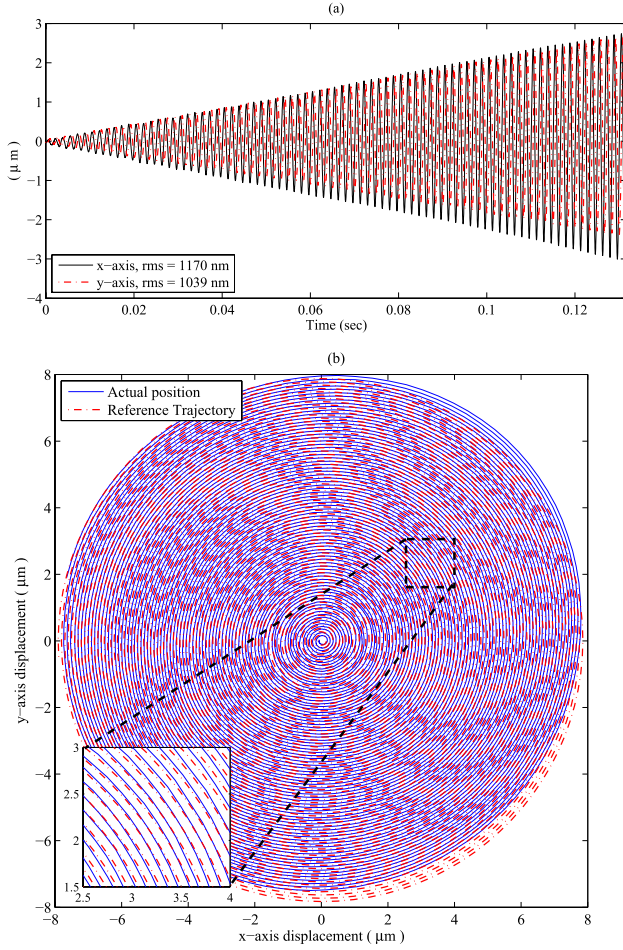
Fig. 9. (a) Profiles of tracking errors after simultaneous application of 600-Hz spiral actuation signals in the open-loop test. (b) Reference trajectory and the actual trajectory of the stage in the open-loop test.

at least a single pair of imaginary poles at f ($\pm i\omega$), the plant dynamics are linear time invariant and the feedback loop is stable, then the tracking error will converge to zero in the presence of sinusoidal exogenous signals at f with constant amplitudes [7]. If the feedback loops with such IMCs have fast transient dynamics, acceptable tracking performances are expected for a spiral trajectory whose amplitude changes slowly. Considering the linear actuation system and the close similarities between the simulated and experimental results reported in Section III, the plant can be considered fairly linear. Hence, it is plausible to examine a conventional IMC with minimum degree as the intermediate IMC, having only one pair of imaginary poles at f.

To design the IMC for the damped plant, we apply an affine parameterization approach for stable plants [29]. The controller is first selected in the following form:

$$C(s) = \frac{D(s)B(s)}{D_i(s)A(s)} \tag{6}$$

where $D(s)$ is the plant model denominator in (5), $D_i(s)$ is a polynomial with poles corresponding to those of the desired exogenous signals, and $A(s)$ and $B(s)$ are polynomials with
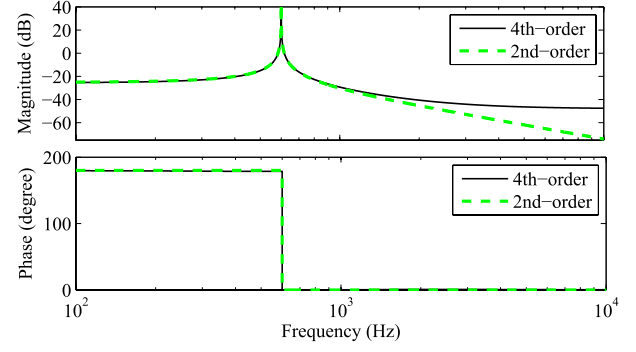

Fig. 10. Frequency responses of the first IMC and its reduced-order approximation.

coefficients to be determined

$$D_i(s) = s^2 + \omega^2 \tag{7}$$

$$B(s) = b_1 s + b_0 \tag{8}$$

$$A(s) = s^2 + a_1 s + a_0 \tag{9}$$

where $\omega = 2\pi f$. Since the damped plant has desirable stable poles, the pole–zero cancelation between the plant and IMC is not only permitted but also reduces the order of loop gain transfer $L(s) = C(s)G(s) = (N(s)B(s)/D_i(s)A(s))$ by 3, reducing the order of the closed-loop characteristic polynomial. We have also selected the orders of unknown polynomials $A(s)$ and $B(s)$ such that the controller is proper and has enough degrees of freedom to assign desirable closed-loop poles from the following polynomial Diophantine equation:

$$A(s)D_i(s) + B(s)N(s) = E(s) \tag{10}$$

where $E(s)$ is the desired characteristic polynomial of the closed-loop system in the following form:

$$E(s) = s^4 + \alpha_3 s^3 + \alpha_2 s^2 + \alpha_1 s + \alpha_0. \tag{11}$$

With $f = 600$ Hz and the desired closed-loop poles reported in Table I, the unknown coefficients a_0, a_1, b_0, and b_1 are determined from the Diophantine equation (10). The desired poles should be selected appropriately (not too fast) to achieve a controller with small gain at high frequencies with acceptable stability margins and closed-loop transient performance. Using (6), we obtain the following IMC:

$$C(s) = \frac{0.004[(s+3190)^2+3687^2](s+13375)(s-13576)}{(s^2+\omega^2)[(s+3239)^2+3559^2]}. \tag{12}$$

Using balanced realization, the reduced-order approximation of the IMC (12) is selected as the intermediate IMC

$$C_i(s) = \frac{-0.055}{1 + \frac{s^2}{\omega^2}}. \tag{13}$$

The frequency responses of IMC (12) and its approximation match well up to a 1-kHz bandwidth, as shown in Fig. 10, and have similar stability margins as reported in Table I. Using the reduced-order controller, the experimental and simulated responses of the closed-loop system to a positive step signal

TABLE I

SELECTED CLOSED-LOOP POLES FOR CONTROLLERS DESIGNED BY THE AFFINE PARAMETERIZATION METHOD AT VARIOUS STEPS OF EACH DESIGN PROCESS FOR TRACKING OF SPIRAL REFERENCES AT DIFFERENT FREQUENCIES. ALSO REPORTED ARE PHASE AND GAIN MARGINS OF EACH CONTROLLER, AS WELL AS SETTLING TIME OF THE CLOSED-LOOP STEP RESPONSE WITHIN 2% OF ITS FINAL VALUE

| Controller Name	Selected poles / (2π) (kHz)	Before model reduction			After model reduction		
		Gain margin (dB)	Phase margin (degree)	Settling time (ms)	Gain margin (dB)	Phase margin (degree)	Settling time (ms)
$C_0(s)$	$-0.17, -0.44 \pm 0.47i$	17.1	75.8	4.6	15.2	74	5
For 600 Hz Spiral Reference							
$C_i(s)$	$-0.126 \pm 0.66i, -0.39 \pm 0.37i$	8.3	-71.3	5.3	8	-69.5	5.3
$C_2(s)$	$-0.1 \pm 1.24i, -0.38 \pm 0.42i$	8.7	75	5.2	8.8	57	6.2
$C_1(s)$	$-0.06 \pm 0.33i, -0.1 \pm 0.62i$ $-0.17 \pm 0.99i, -1.66 \pm 0.99i, -2.53$	9.5	-20	12.7	9.5	-20	12.7
$C_f(s)$	N/A	N/A	N/A	N/A	7.2	-24.6	13.3
For 1430 Hz Spiral Reference							
$C_1'(s)$	$-0.1 \pm 1.58i, -0.4 \pm 0.12i$	2.8	42.3	2.9	2.8	41	3.1
$C_1(s)$	$-0.06 \pm 1.4i, -0.2 \pm 1.1i$ $-0.6 \pm 0.95i, -1.4, -5, -10$	5.5	-17.2	8.2	5.5	-17.2	8.2
$C_i(s)$	N/A	N/A	N/A	N/A	5.2	43.7	5.9
$C_f(s)$	N/A	N/A	N/A	N/A	3.8	-18.9	5.3
For 240 Hz Spiral Reference							
$C_2(s)$	$-0.29 \pm 0.54i, -0.26 \pm 0.36i$	5.9	-48.1	3.5	5.8	-48	3.5
$C_3(s)$	$-0.01 \pm 0.73i, -0.14 \pm 0.4i$ $-0.32 \pm 0.83i, -2.2, -5, -10$	6	-28.4	5.3	6	-28	5.3
$C_1(s)$	$-0.004 \pm 0.24i, -0.12 \pm 0.44i$ $-0.26, -0.61, -2, -5, -10$	7	33.7	10.8	7	33.9	10.7
$C_f(s)$	N/A	N/A	N/A	N/A	2.8	28.4	13.6
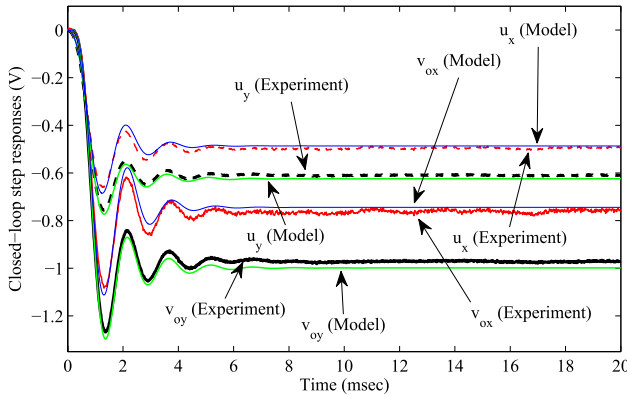
Fig. 11. Closed-loop responses to a 1.5 V step at the reference with the second-order IMC in (13). For the simulation results of the x-axis, the dc gain of the plant model (1) was reduced to 1.53.
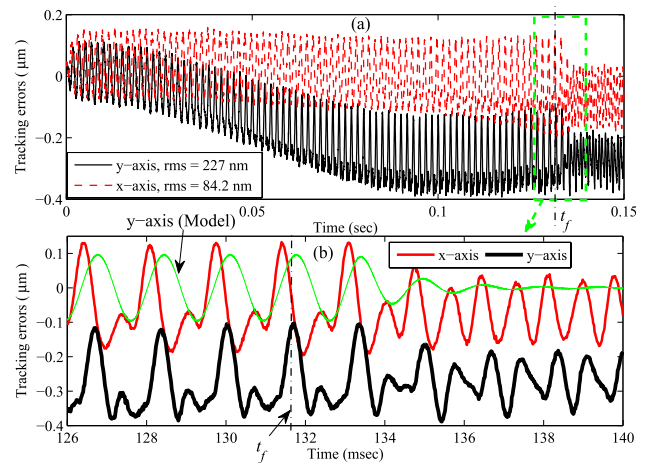

Fig. 12. Performance of the intermediate IMC in simultaneous tracking of spiral references by both axes at the frequency of 600 Hz. The root-mean-square (rms) values of the errors are associated with the scan period of $t_f = 131.67$ ms. After the scan period ($t = t_f$), the error fluctuations are clearly reduced for both axes. (b) is a close-up view of figure (a) around $t = t_f$.

with a height of 1.5 V indicate an acceptable settling time of 5.3 ms, as shown in Fig. 11. The differences between the steady-state values in the experiments and the model are related to deviations of the plant dc gains from the nominal value of 1.6, which are 1.53 and 1.58 for the x- and y-axis, respectively.

We now evaluate the tracking performance of the spiral reference described in Section IV at the frequency of 600 Hz, which corresponds to a scan period of 131.7 ms. Applying the intermediate IMC for simultaneous tracking of the spiral waveforms, we obtained the experimental tracking errors reported in Fig. 12. During the scan period ($t < t_f$), when the reference amplitudes are increasing, the tracking errors have larger amplitudes compared with the constant amplitude interval at the end. In addition, the errors gradually increase in amplitude and their moving averages drift away from the

original values, while the reference amplitude rises. As shown in the close-up view, each error contains a dominant fundamental frequency component (600 Hz) during the scan period, which is considerably reduced after the reference amplitude is kept constant, leaving the second and third harmonics as the dominant components. The residual higher order harmonics are mainly due to plant nonlinearities such as cross coupling between the two axes and minor asymmetries from nonzero fabrication tolerances. Using the linear model of the plant in continuous time, we also carried out a hybrid simulation for the y-axis, in which the controllers are discretized by the sampling rate used during the experiment (60 kHz).

The simulated tracking error is also included in Fig. 12(b), showing a steady sinusoidal error at the fundamental frequency during the scan, which rapidly dies out after the scan, when the reference amplitude stops changing. The spiral reference signals described by (2) and (3) have purely imaginary poles at $\pm i\omega$, which are repeated twice. This is revealed by considering the following Laplace transforms:

$$\mathcal{L}[(1 + \alpha t)\cos(\omega t)] = \frac{s(s^2 + \omega^2) + \alpha(s^2 - \omega^2)}{(s^2 + \omega^2)^2} \quad (14)$$

$$\mathcal{L}[(1 + \alpha t)\sin(\omega t)] = \frac{\omega(s^2 + \omega^2) + 2\alpha\omega s}{(s^2 + \omega^2)^2} \quad (15)$$

and the fact that no pole–zero cancelation will occur in (14) and (15) if the rate of amplitude variation (α) is not zero. Hence, the simulation reveals that the larger amplitude of the error during the scan is primarily due to the fact that each controller has only one pair of imaginary poles at the frequency of the spiral reference signals.

B. Final Controller for 600 Hz

To reduce the amplitude of the fundamental component in the tracking error during the spiral scan, we need to incorporate at least two pairs of imaginary poles at the frequency of reference ($\pm i\omega$ repeated twice) into the IMC. Dominant higher order harmonics in the error may also need to be canceled by including additional purely imaginary poles at the second and/or third harmonics of the reference frequency ($\pm 2i\omega$, $\pm 3i\omega$). In addition, due the undesirable drift of the tracking error, we will finally need to add an integrator to the controller (pole at 0). However, as the number of marginally stable poles in the IMC increases, the resulting closed-loop system generally has lower stability margins and exhibits a less desirable transient performance.

When using affine parameterization or other pole assignment approaches to design an IMC, as the number of internal model modes increases, the order of the characteristic equation increases. Consequently, we may face the difficult task of selecting a high number of desired closed-loop poles at appropriate locations in an unlimited region (left half-plane) to attain acceptable robustness and transient performance.

To avoid this difficulty, we partition the controller design process into several steps, each involving only one of the required internal modes. In each step, the order of the characteristic equation associated with a minimal-order controller is considerably lower than that of the overall modes, making the controller design process more straightforward. For each internal model mode, we design an individual minimal-order IMC that satisfies acceptable stability, robustness, and transient performances. The final IMC, which contains all the required modes, is simply determined by a linear combination of the individual controllers with coefficients that can be easily tuned in a small range ([0, 1]).

For the first step, we design an IMC with only one integrator, which is the simplest internal model mode among the required modes. Using the design approach of Section V-A, the minimal proper controller is selected as (6) with $D_i(s) = s$, $B(s) = b_0$, and $A(s)$ as in (9). The three unknown

coefficients a_1, a_0, and b_0 are obtained from (10), where $E(s)$ is a monic third-order polynomial whose coefficients are determined from the desired poles reported in Table I. The resulting third-order controller is then reduced to the following first-order controller:

$$C_0 = \frac{100}{s}. \quad (16)$$

When inserted as an IMC in the second loop, controller (16) provides the acceptable stability margins and settling time reported in Table I.

In the next step, we design an IMC with only one pair of imaginary poles at the second harmonic of the 600-Hz reference frequency, which is the dominant component in the experimental errors after the scan period in Fig. 12(b). The design procedure is as outlined in Section V-A for the controller with a pair of imaginary poles at the fundamental frequency. After model reduction, the resulting IMC for rejection of the second harmonic in the error is as

$$C_2(s) = -\frac{8.3 \times 10^{-6}s + 0.05}{1 + \frac{s^2}{4\omega^2}} \quad (17)$$

where the selected closed-loop poles, stability margins, and settling time associated with (17) are reported in Table I.

In the third step, we design an IMC with minimal order with exactly two pairs of purely imaginary poles at the fundamental frequency of the spiral reference. If we try the design procedure of Section V-A, we can obtain sixth-order controllers in the form of (6) by selecting $A(s)$ as in (9) and $B(s)$ and $D_i(s)$ as

$$D_i(s) = (s^2 + \omega^2)^2 \quad (18)$$
$$B(s) = b_3 s^3 + b_2 s^2 + b_1 s + b_0 \quad (19)$$

where the six unknown coefficients in $A(s)$ and $B(s)$ are determined from the Diophantine equation (10), after selecting six stable closed-loop poles of the monic polynomial $E(s)$ at appropriate locations. However, the controllers obtained by this approach could not satisfy large stability margins and acceptable settling times simultaneously. A reason for this limitation can be attributed to the fact that the controllers in the form of (6) have three fixed zeros exactly equal to the plant poles ($D(s)$), which limit the number of degrees of freedom for a sixth-order proper controller with four poles fixed at $\pm i\omega$. To obtain controllers with larger stability margins and acceptable settling time, we provide more degrees of freedom without increasing the controller degree by eliminating the fixed factor $D(s)$ in (6) as

$$C(s) = \frac{B(s)}{D_i(s)A(s)} \quad (20)$$

where $A(s)$ and $D_i(s)$ are as before (9), (18) and $B(s)$ is given by

$$B(s) = \sum_{k=0}^{6} b_k s^k. \quad (21)$$

Since the pole–zero cancelation in the previous approach does not occur, the resulting Diophantine equation is given by

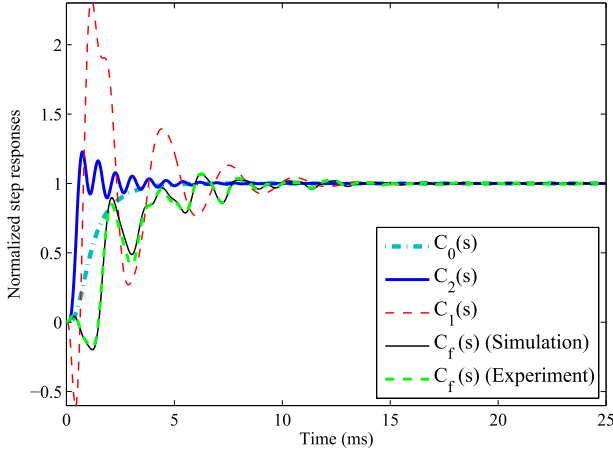$$A(s)D_i(s)D(s) + B(s)N(s) = E(s) \quad (22)$$

Fig. 13. Simulated step responses normalized by their steady-state values, when the IMCs designed in each step are individually used to close the second loop. The result of the final IMC is also included along with the corresponding experimental result for the y-axis.

where $E(s)$ is a monic polynomial of order 9, whose poles are assigned based on desired stable closed-loop performances. Selecting the poles reported in Table I, we obtain a sixth-order controller from (20), which can be reduced to the following fourth-order one:

$$C_1(s) = \frac{0.12s^4 - 50s^3 + 10^6 s^2 - 3.1 \times 10^9 s - 9.2 \times 10^{12}}{(s^2 + \omega^2)^2}.$$
(23)

The resulting closed-loop stability margins and settling time associated with this controller are also reported in Table I. It is also important to calculate the controller zeros (3073, -1677, $-490 \pm 3823i$ rad/s) to ensure that they do not overlap with any of the required internal model poles.

The final IMC, which includes all the intended internal modes, can be determined from a linear combination of the individual controllers as

$$C_f(s) = c_0 C_0(s) + c_1 C_1(s) + c_2 C_2(s). \quad (24)$$

The coefficients in (24) are empirically selected within a limited positive range. Hence, they are assigned much more conveniently than choosing many stable closed-loop poles in the complex plane as a result of including all the internal model modes into the control design process at once. Assuming $c_1 = c_2 = 0.25$ and $c_0 = 0.5$, the closed-loop specifications of the control system with the final controller are acceptable, as reported in Table I. The zeros of the final controller are $1090 \pm 6427i$, -4133, $-444 \pm 3768i$, 3005, and 2519 rad/s, which do not overlap with any of the internal model poles. The closed-loop step response of the control system with each individual IMC is shown in Fig. 13, where each response has been divided by its steady-state value. Also included in Fig. 13, are the simulated and experimental results using the final IMC in the feedback system (24), which are matching well. The close responses obtained through simulation and experiment confirm the use of simulation for fine tuning of the coefficients in (24) before implementing the final controller on the actual system, which is a favorable approach that prevents damage due to instability. The phase and gain margins of the final
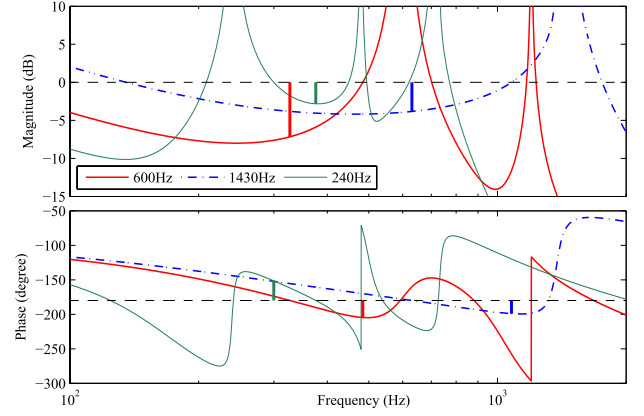

Fig. 14. Frequency responses of the loop gain with the final IMCs for reference frequencies 600, 1430, and 240 Hz. The thick solid lines with the same color as each plot indicate the gain and phase margins. Due to the purely imaginary poles of the IMCs, the peaks are not visible in the magnitude graphs.
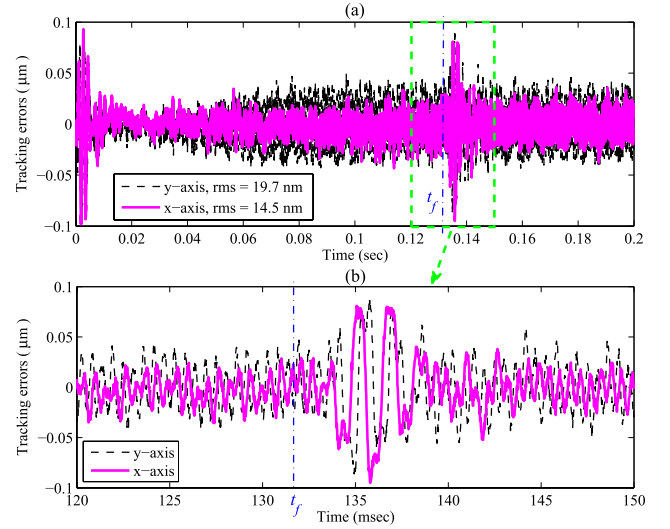

Fig. 15. Performance of the final IMC in simultaneous tracking of spiral references by both axes at the frequency of 600 Hz and scan period of 131.67 ms. (b) is a close-up view of figure (a) around $t = t_f$.

controller are also indicated in the Bode diagram of the loop gain in Fig. 14.

Fig. 15 shows the resulting experimental performance of the final IMC in tracking of the previously mentioned 600-Hz spiral references. The dramatic improvements in the tracking errors compared with those of the intermediate IMC in Fig. 12 demonstrate that the additional internal model modes incorporated into the controller have been very effective in improving the control performance of the spiral scan trajectory. A small steady vibration with frequency of 1800 Hz is visible in the tracking errors shown in Fig. 15(b), which is expected as we did not include any internal modes at the third harmonic of the reference frequency. Also shown in Fig. 8(b) is the resulting trajectory of the stage position, which is closely tracking the spiral reference trajectory.

C. Spiral Trajectory Tracking at 1430 Hz

To address the performance of the proposed IMC design approach in the tracking of spiral waveforms at a
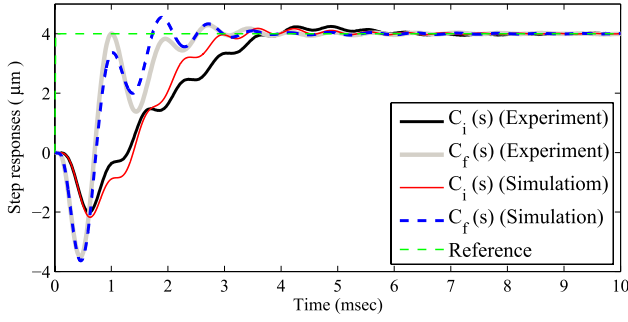
Fig. 16. Experimental step responses when the final IMCs are individually used to close the second loop for the y-axis. Using the same step references and discretizing the IMC and damping controllers with the same sampling interval used in the experiments (60 kHz), the results of hybrid simulation of the closed-loop systems with the continuous plant model (1) are also included.

higher speed ($f = 1430$ Hz), we designed intermediate and final controllers, which have one and two pairs of imaginary poles at $\pm i\omega$, respectively, in addition to one pole at $s = 0$. Since an individual integral controller (16) has already been designed, we first designed two controllers $C_1'(s)$ and $C_1(s)$ with only one and only two pairs of the imaginary poles, using the approaches mentioned in Sections V-A and V-B, respectively. The intermediate and final IMCs are then obtained by linearly combining the integral controller C_0 with either $C_1'(s)$ or $C_1(s)$ as

$$C_i(s) = 0.55C_1'(s) + 0.6C_0(s) \tag{25}$$

$$C_f(s) = C_1(s) + C_0(s) \tag{26}$$

where

$$C_1'(s) = -0.1\frac{\left(1 + \frac{s}{6410}\right)}{\left(1 + \frac{s^2}{\omega^2}\right)} \tag{27}$$

$$C_1(s) = -0.041\frac{\left(1 + \frac{0.0668s}{8638} + \frac{s^2}{8638^2}\right)\left(1 + \frac{1.445s}{3674} + \frac{s^2}{3674^2}\right)}{\left(1 + \frac{s^2}{\omega^2}\right)^2}. \tag{28}$$

The closed-loop poles selected during the design of controllers $C_1'(s)$ and $C_1(s)$ are reported in Table I along with their stability margins and settling times, when inserted in the second loop individually. Also included in Table I are the closed-loop attributes of the system with the final IMCs. Fig. 16 shows the step responses of the final closed-loop systems obtained by experiment and hybrid simulations.

Fig. 17 shows the experimental error profiles with the final IMCs, when spiral references at the frequency of 1430 Hz are simultaneously applied to both axes with the same magnitude and pitch values as before. The considerable improvement in the tracking errors obtained by the final controller with respect to the intermediate controller further indicates the efficacy of incorporating two pairs of imaginary poles at the frequency of the spiral reference into the controllers.

D. Spiral Trajectory Tracking at 240 Hz

As will be explained in the next section, a bandwidth limitation of the z-axis in the AFM requires us to select the
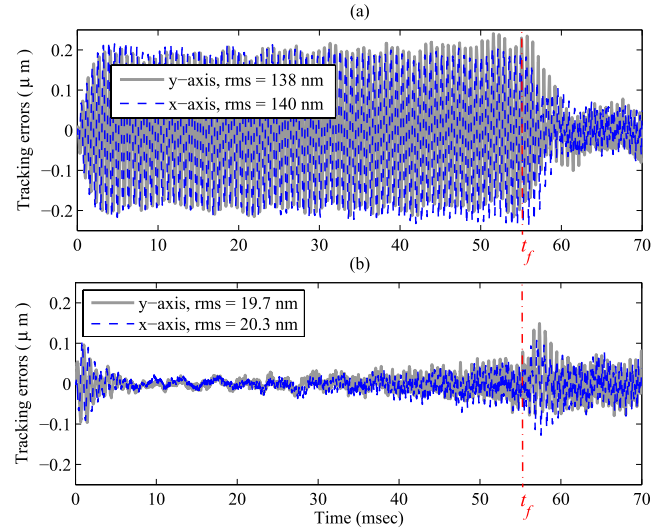

Fig. 17. Experimental tracking performances of the two IMCs in simultaneous tracking of spiral references by both axes at the frequency of 1430 Hz and scan period of $t_f = 55.24$ ms. (a) Intermediate controller. (b) Final controller.

frequency of the spiral references much lower than 600 Hz. In this section, we design an intermediate and a final IMC for spiral references at $f = 240$ Hz. Previous experimental testing with the MEMS nanopositioner has shown that the device's nonlinearity is more severe at lower frequencies, and we therefore include internal model poles at both the second and third harmonics of the reference frequency. For the intermediate controller, we included two pairs of poles at $\pm i\omega$, one pair at $\pm 2i\omega$ and $\pm 3i\omega$, and one pole at $s = 0$. However, the resulting tracking errors for spiral references with the same amplitude and pitch values as before were not acceptable, as shown in Fig. 18. The time profiles indicate that the amplitudes of the third harmonic components within the errors increase during the scan period. Hence, we included two pairs of poles at $\pm 3i\omega$ into the final IMC, increasing the order of controller to 11. The final IMC is also obtained from a linear combination of individual controllers as

$$C_f(s) = 0.3C_1(s) + 0.15C_2(s) + 0.3C_0(s) + 0.35C_3(s) \tag{29}$$

where C_0 is the integral controller in (16) and

$$C_1(s) = -0.0123\frac{\left(1 - \frac{s}{127.5}\right)\left(1 + \frac{0.0276s}{1504} + \frac{s^2}{1504^2}\right)}{\left(1 + \frac{s^2}{\omega^2}\right)^2} \tag{30}$$

$$C_2(s) = \frac{-0.07}{1 + \frac{s^2}{4\omega^2}} \tag{31}$$

$$C_3(s) = -0.0684\frac{\left(1 + \frac{s}{3871}\right)\left(1 + \frac{0.026s}{4598} + \frac{s^2}{4598^2}\right)}{\left(1 + \frac{s^2}{9\omega^2}\right)^2}. \tag{32}$$

To design $C_2(s)$, we applied the method mentioned in Section V-A. For $C_1(s)$ and $C_3(s)$, the design approach proposed in Section V-B was used. The details of the selected closed-loop poles for each individual controller and the resulting closed-loop attributes have been summarized in Table I,
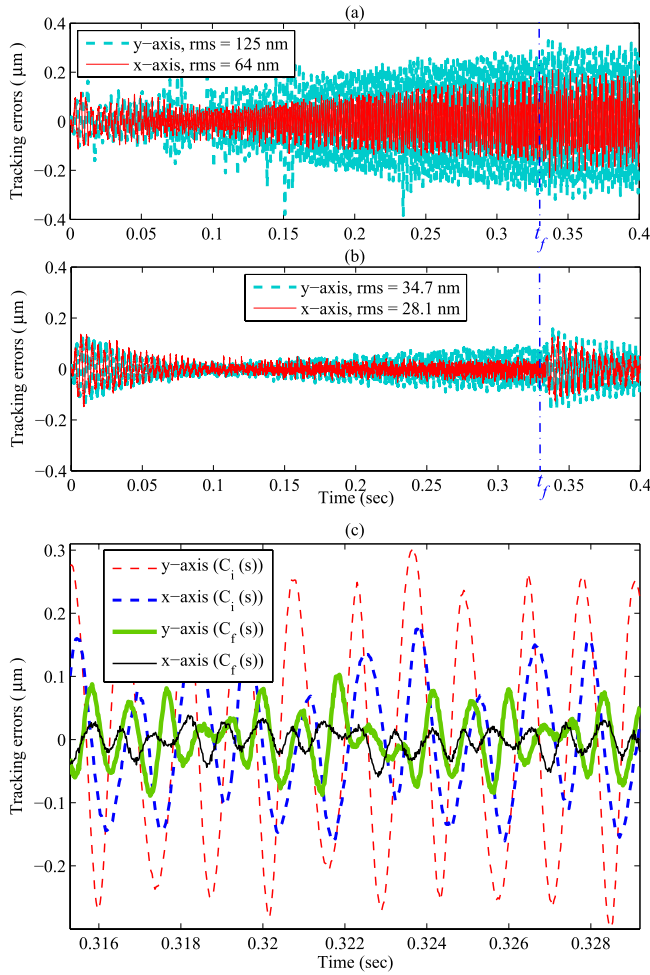
Fig. 18. Experimental tracking performances of the two IMCs in simultaneous tracking of spiral references by both axes at the frequency of 240 Hz and scan period of $t_f = 0.329$ s. (a) Intermediate controller. (b) Final controller. (c) Close-up view of the tracking error around $t = t_f$.
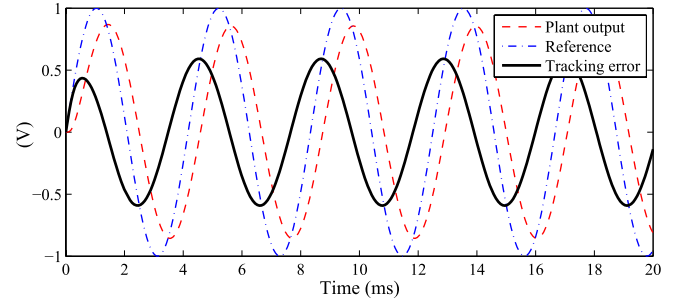

Fig. 19. Simulation results of tracking a 240-Hz sinusoidal reference by a PID controller.
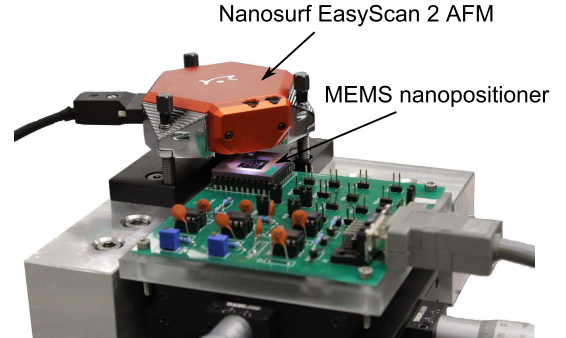

Fig. 20. Experimental setup of MEMS nanopositioner and Nanosurf EasyScan 2 AFM for imaging using a spiral scan trajectory.

as well as those of the final IMC $C_f(s)$. The tracking errors obtained by the final controller are also included in Fig. 18. Clearly, incorporating repeated poles at $\pm 3i\omega$ into the final controller has considerably attenuated the third-harmonic component of the tracking error compared with that of the intermediate controller. With the final controller, the residual dominant component of the error profiles in Fig. 18(c) corresponds to the fifth harmonic of the reference, whose poles have not been included in the final controller. However, since the magnitude of the errors are mostly below the spiral pitch (0.1 μm) during the scan period, we did not include the fifth mode in the controller.

Remark 1: To reduce the effect of sensor noise feedback on the actual displacement, the control system should have a low closed-loop bandwidth. A significant characteristic of the IMCs is that they achieve considerably good tracking performance for a group of desired reference signals without imposing a high closed-loop bandwidth. The closed-loop bandwidth of the system with the final IMC for the 240-Hz spiral trajectory is about 64 Hz, while the amplitude of the tracking error is approximately 1/80 of the spiral reference

amplitude. Such a tracking performance is not achievable by traditional control methods such as PID, which are usually designed to track band-limited reference signals. For example, if we replace the IMC in Fig. 6 by a well-tuned PID controller such as $0.094 + (300/s) + 1.626 \times 10^{-5}$ s, the resulting closed-loop system will have the much larger bandwidth of 400 Hz. However, the tracking performance of this PID controller with a 240 Hz sinusoidal reference is still not acceptable, as shown in the simulation in Fig. 19.

VI. AFM IMAGING

The periodic gold features fabricated on the surface of the stage are used as scan samples to test the performance of the closed-loop nanopositioner by obtaining an AFM image using the spiral scanning method. The features measure $9 \times 3 \times 0.5$ μm and are shown in a close-up view in Fig. 1. As shown in Fig. 20, the packaged MEMS device is mounted on a printed circuit board on which sensing and actuating circuits are constructed. The scan is performed by utilizing the cantilever and associated deflection sensor of a Nanosurf EasyScan2 AFM, which is positioned in such a way that the cantilever can be landed on the stage of the MEMS nanopositioner.

The contact mode scanning method is chosen to perform the imaging using a cantilever with a resonance frequency of 13 kHz. Due to the low bandwidth of the AFM's z-axis positioner, a constant height mode is adopted where the base of the cantilever remains stationary with respect to the sample. In this scanning condition, however, at high scan speeds, the cantilever is prone to oscillations, which lead to the occurrence of artifacts in the obtained image, and there is increased potential for the cantilever's tip and/or the
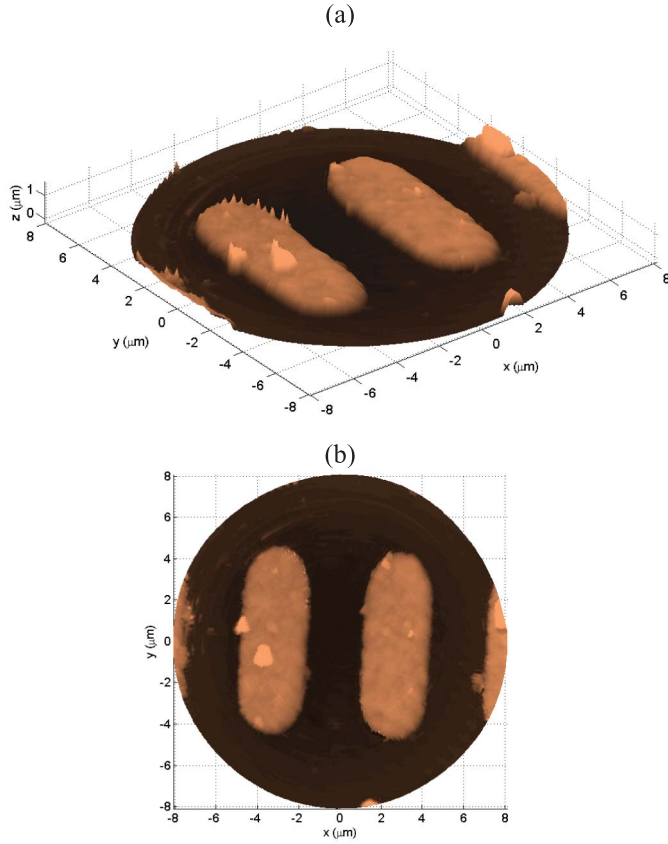
(a)

(b)

Fig. 21. AFM image of gold features on the stage of MEMS nanopositioner, obtained using a spiral scanning trajectory with $f = 240$ Hz. (a) 3-D. (b) 2-D.

sample being damaged due to lateral impacts with the sample features. Hence, the desire to obtain artifact free images places a limitation on the maximum spiral scanning frequency. For an imaging window with a diameter of 16 μm, the maximum spiral scan frequency attainable while maintaining good image quality was experimentally determined to be $f = 240$ Hz. In Fig. 21, the resulting AFM image of the gold structures on the stage obtained at this frequency is shown. The 3-D topography of the gold features is constructed from the cantilever deflection signal provided by the AFM's built-in laser sensor and in-plane displacement measurements recorded from the nanopositioner's electrothermal sensors.

In spite of the nanopositioner's excellent spiral trajectory tracking performance at higher frequencies, as reported in Sections V-B and V-C, the imaging at spiral reference frequencies of 600 Hz and 1430 Hz was not possible for the reasons described above. As a potential area for future development, a fast z-axis nanopositioner for the cantilever should be implemented to make scanning in constant-force contact mode feasible at higher speeds such as 600 and 1430 Hz.

VII. CONCLUSION

We achieved accurate tracking of spiral scan trajectories with constant angular velocity by designing IMCs that include two pairs of imaginary poles at the frequency of the reference signals. The method was implemented on a novel 2-D MEMS nanopositioner equipped with built-in electrothermal sensors,

comb drives, and linear actuation mechanisms. To reduce the tracking error resulting from plant nonlinearities, it is also required to include an integrator (a pole at the origin) plus imaginary poles corresponding to the second and/or third harmonics of the reference frequency into the IMC. To simplify the control design process, individual controllers are designed by affine parameterization approaches with minimum degrees, each involving only one of the intended modes to facilitate the pole assignment process. The final controller can be easily tuned as a linear combination of the individual controllers with positive coefficients in the range [0, 1], ensuring a minimal order for the controller with all intended modes included. The effectiveness of the proposed approach in tracking of an aggressive spiral trajectory with high diameter and pitch values (16 μm and 100 nm, respectively) was demonstrated at three different frequencies with the maximum value (1430 Hz) exceeding the dominant resonance frequency of the nanopositioner, achieving a video frame rate of 18 frames/s. The applicability of the controlled device for on-chip AFM was also addressed by landing a commercial AFM cantilever on the stage and capturing an image of fabricated gold features on the stage, while following the spiral trajectory at 240 Hz.

REFERENCES

[1] S. Akamine, T. R. Albrecht, M. J. Zdeblick, and C. F. Quate, "Micro-fabricated scanning tunneling microscope," *IEEE Electron Device Lett.*, vol. 10, no. 11, pp. 490–492, Nov. 1989.

[2] Y. Xu, N. C. MacDonald, and S. A. Miller, "Integrated micro-scanning tunneling microscope," *Appl. Phys. Lett.*, vol. 67, no. 16, pp. 2305–2307, Oct. 1995.

[3] S. Hafizovic, K.-U. Kirstein, and A. Hierlemann, *Integrated Cantilevers and Atomic Force Microscopes*, *Applied Scanning Probe Methods V* (Scanning Probe Microscopy Techniques). Berlin, Germany: Springer-Verlag, 2007, ch. 1, pp. 1–22.

[4] N. Sarkar, R. R. Mansour, O. Patange, and K. Trainor, "CMOS-MEMS atomic force microscope," in *Proc. 16th Int. Solid-State Sens., Actuators Microsyst. Conf. (TRANSDUCERS)*, Jun. 2011, pp. 2610–2613.

[5] M. Azizi, N. Sarkar, and R. R. Mansour, "Single-chip CMOS-MEMS dual mode scanning microwave microscope," *IEEE Trans. Microw. Theory Techn.*, vol. 61, no. 12, pp. 4621–4629, Dec. 2013.

[6] P. Vettiger *et al.*, "The 'millipede'—Nanotechnology entering data storage," *IEEE Trans. Nanotechnol.*, vol. 1, no. 1, pp. 39–55, Mar. 2002.

[7] A. G. Fowler, M. Maroufi, A. Bazaei, and S. O. R. Moheimani, "MEMS nanopositioner for Lissajous-scan atomic force microscopy," in *Proc. ASME Dyn. Syst. Control Conf.*, San Antonio, TX, USA, Oct. 2014, pp. V003T44A004-1–V003T44A004-5.

[8] A. Mohammadi, A. G. Fowler, Y. K. Yong, and S. O. R. Moheimani, "A feedback controlled MEMS nanopositioner for on-chip high-speed AFM," *J. Microelectromech. Syst.*, vol. 23, no. 3, pp. 610–619, Jun. 2014.

[9] M. Maroufi, A. Bazaei, and S. O. R. Moheimani, "A high-bandwidth MEMS nanopositioner for on-chip AFM: Design, characterization, and control," *IEEE Trans. Control Syst. Technol.*, vol. 23, no. 2, pp. 504–512, Mar. 2015.

[10] R. Wiesendanger, *Scanning Probe Microscopy and Spectroscopy: Methods and Applications*. Cambridge, U.K.: Cambridge Univ. Press, 1994.

[11] B. Bhushan, Ed., *Springer Handbook of Nanotechnology*, 3rd ed. Berlin, Germany: Springer-Verlag, 2010.

[12] I. A. Mahmood and S. O. R. Moheimani, "Fast spiral-scan atomic force microscopy," *Nanotechnology*, vol. 20, no. 36, 2009, Art. ID 365503.

[13] Y. K. Yong, S. O. R. Moheimani, and I. R. Petersen, "High-speed cycloid-scan atomic force microscopy," *Nanotechnology*, vol. 21, no. 36, p. 365503, 2010.

[14] A. Bazaei, Y. K. Yong, and S. O. R. Moheimani, "High-speed Lissajous-scan atomic force microscopy: Scan pattern planning and control design issues," *Rev. Sci. Instrum.*, vol. 83, no. 6, pp. 063701-1–063701-10, 2012.

[15] T. Tuma, J. Lygeros, V. Kartik, A. Sebastian, and A. Pantazi, "High-speed multiresolution scanning probe microscopy based on Lissajous scan trajectories," *Nanotechnology*, vol. 23, no. 18, p. 185501, 2012.

[16] I. A. Mahmood, S. O. R. Moheimani, and B. Bhikkaji, "A new scanning method for fast atomic force microscopy," *IEEE Trans. Nanotechnol.*, vol. 10, no. 2, pp. 203–216, Mar. 2011.

[17] Y. K. Yong, S. O. R. Moheimani, B. J. Kenton, and K. K. Leang, "Invited review article: High-speed flexure-guided nanopositioning: Mechanical design and control issues," *Rev. Sci. Instrum.*, vol. 83, no. 12, p. 121101, 2012.

[18] S. Devasia, E. Eleftheriou, and S. O. R. Moheimani, "A survey of control issues in nanopositioning," *IEEE Trans. Control Syst. Technol.*, vol. 15, no. 5, pp. 802–823, Sep. 2007.

[19] B. Bhikkaji, M. Ratnam, A. J. Fleming, and S. O. R. Moheimani, "High-performance control of piezoelectric tube scanners," *IEEE Trans. Control Syst. Technol.*, vol. 15, no. 5, pp. 853–866, Sep. 2007.

[20] H. Habibullah, H. R. Pota, and I. R. Petersen, "High-speed spiral imaging technique for an atomic force microscope using a linear quadratic Gaussian controller," *Rev. Sci. Instrum.*, vol. 85, no. 3, p. 033706, 2014. [Online]. Available: http://dx.doi.org/10.1063/1.4868249

[21] M. S. Rana, H. R. Pota, and I. R. Petersen, "Spiral scanning with improved control for faster imaging of AFM," *IEEE Trans. Nanotechnol.*, vol. 13, no. 3, pp. 541–550, May 2014.

[22] H. Habibullah, H. R. Pota, and I. R. Petersen, "Phase-locked loop-based proportional integral control for spiral scanning in an atomic force microscope," in *Proc. 19th IFAC World Congr.*, Aug. 2014, pp. 6563–6568.

[23] B. A. Francis and W. M. Wonham, "The internal model principle of control theory," *Automatica*, vol. 12, no. 5, pp. 457–465, 1976.

[24] Y. K. Yong, A. Bazaei, and S. O. R. Moheimani, "Video-rate Lissajous-scan atomic force microscopy," *IEEE Trans. Nanotechnol.*, vol. 13, no. 1, pp. 85–93, Jan. 2014.

[25] A. Cowen, G. Hames, D. Monk, S. Wilcenski, and B. Hardy, *SOIMUMPs Design Handbook*, 8th ed. Durham, NC, USA: MEMSCAP Inc., 2011. [Online]. Available: http://www.memscap.com/products/mumps/soimumps/reference-material

[26] M. Maroufi, A. G. Fowler, A. Bazaei, and S. O. R. Moheimani, "High-stroke silicon-on-insulator MEMS nanopositioner: Control design for non-raster scan atomic force microscopy," *Rev. Sci. Instrum.*, vol. 86, no. 2, pp. 023705-1–023705-12, 2015.

[27] D. Sidobre and V. Hayward, "Calibrated measurement of the behaviour of mechanical junctions from micrometre to subnanometre scale: The friction force scanner," *Meas. Sci. Technol.*, vol. 15, no. 2, pp. 451–459, 2004.

[28] A. G. Fowler, A. Bazaei, and S. O. R. Moheimani, "Design and analysis of nonuniformly shaped heaters for improved MEMS-based electrothermal displacement sensing," *J. Microelectromech. Syst.*, vol. 22, no. 3, pp. 687–694, Jun. 2013.

[29] G. C. Goodwin, S. F. Graebe, and M. E. Salgado, *Control System Design*. Englewood Cliffs, NJ, USA: Prentice-Hall, 2001.

Mohammad Maroufi (S'14) received the B.Sc. degree in mechanical engineering and applied physics and the master's degree in mechatronics from the Amirkabir University of Technology, Tehran, Iran, in 2008 and 2011, respectively, and the Ph.D. degree in electrical engineering from The University of Newcastle, Callaghan, NSW, Australia.

He is currently a Research Associate with the Department of Mechanical Engineering, The University of Texas at Dallas, Richardson, TX, USA. His current research interests include the design and control of microelectromechanical systems (MEMS) nanopositioning systems, MEMS-based sensing and actuation, on-chip atomic force microscopy, and modeling of smart materials and structures.

Anthony G. Fowler (S'10–M'15) received the bachelor's and Ph.D. degrees in electrical engineering from The University of Newcastle, Callaghan, NSW, Australia, in 2010 and 2014, respectively,

He is currently a Post-Doctoral Fellow with the School of Electrical Engineering and Computer Science, The University of Newcastle. He is also a Visiting Researcher with the Department of Mechanical Engineering, The University of Texas at Dallas, Richardson, TX, USA. His current research interests include the design and analysis of novel microelectromechanical systems for energy harvesting, nanopositioning, and scanning probe microscopy applications.

Ali Bazaei (M'10) received the B.Sc. and M.Sc. degrees from Shiraz University, Shiraz, Iran, in 1992 and 1995, respectively, defended a Ph.D. degree at Tarbiat Modares University, Tehran, Iran, in 2004, and received a Ph.D. degree from University of Western Ontario, London, ON, Canada, in 2009, all in electrical engineering.

He was an Instructor with Yazd University, Yazd, Iran, from 1995 to 2000. From 2004 to 2005, he was a Research Assistant with the Department of Electrical and Computer Engineering, University of Western Ontario. He is currently a Post-Doctoral Research Fellow (level B, step five) with the School of Electrical Engineering and Computer Science, The University of Newcastle, Callaghan, NSW, Australia. He has been elected as a Future Science Leader to foster research collaborations between Australia and China through the 2015 Australia China Young Scientists Exchange Program. He has authored over 50 peer-reviewed articles, including the IEEE TRANSACTIONS ON AUTOMATIC CONTROL, *Automatica*, *Systems & Control Letters*, the *ASME Journal of Dynamic Systems Measurement and Control*, the *Journal of Vibration and Control*, the *Journal of Microelectromechanical Systems*, the IEEE TRANSACTIONS ON NANOTECHNOLOGY, the IEEE SENSORS JOURNAL, the IEEE TRANSACTIONS ON MECHATRONICS/*ASME Transactions on Mechatronics*, and *Review of Scientific Instruments*. His current research interests include the general area of nonlinear systems, including control and modeling of structurally flexible systems, friction modeling and compensation, neural networks, and microposition sensors.

S. O. Reza Moheimani (F'11) currently holds the James von Ehr Distinguished Chair in Science and Technology with the Department of Mechanical Engineering, The University of Texas at Dallas, Richardson, TX, USA. His current research interests include ultrahigh-precision mechatronic systems, with a particular emphasis on dynamics and control at the nanometer scale, including applications of control and estimation in nanopositioning systems for high-speed scanning probe microscopy and nanomanufacturing, modeling and control of microcantilever-based devices, control of microactuators in microelectromechanical systems, and design, modeling, and control of micromachined nanopositioners for on-chip scanning probe microscopy.

Dr. Moheimani is a fellow of the International Federation of Automatic Control (IFAC) and the Institute of Physics, U.K. His research has been recognized with a number of awards, including the IFAC Nathaniel B. Nichols Medal in 2014, the IFAC Mechatronic Systems Award in 2013, the IEEE Control Systems Technology Award in 2009, the IEEE TRANSACTIONS ON CONTROL SYSTEMS TECHNOLOGY Outstanding Paper Award in 2007, and several best student paper awards in various conferences. He has served on the Editorial Boards of a number of journals, including the IEEE TRANSACTIONS ON MECHATRONICS, the IEEE TRANSACTIONS ON CONTROL SYSTEMS TECHNOLOGY, and *Control Engineering Practice*. He is the Chair of the IFAC Technical Committee on Mechatronic Systems, and has chaired several international conferences and workshops. He is the Editor-in-Chief of *Mechatronics*.